Photoactive *p*-Type Spinel CuGa$_2$O$_4$ Nanocrystals

Owen Kendall[1], Lesly Melendez-Correa[1], Jiawen Ren[1], Samantha Prabath Ratnayake[1], Billy J. Murdoch[2], Edwin Mayes[2], Joel van Embden, Daniel E. Gomez, Arrigo Calzolari[3,], Enrico Della Gaspera[1,*]*

[1] School of Science, RMIT University, Melbourne VIC 3000, Australia.

[2] RMIT Microscopy and Microanalysis Facility, College of Science, Engineering and Health, RMIT University, Melbourne, VIC 3000, Australia.

[3] CNR-NANO Istituto Nanoscienze, Centro S3, I-4115 Modena, Italy.

Corresponding author: *enrico.dellagaspera@rmit.edu.au, arrigo.calzolari@nano.cnr.it

KEYWORDS: semiconductors, oxides, nanoparticles, gallium, copper.

Abstract

Herein we report the synthesis and characterization of spinel copper gallate (CuGa$_2$O$_4$) nanocrystals (NCs) with an average size of 3.7 nm via a heat-up colloidal reaction. CuGa$_2$O$_4$ NCs have a band gap of ~2.5 eV and strong p-type character, in agreement with ab initio simulations. These novel NCs are demonstrated to be photoactive, generating a clear and reproducible photocurrent under blue light irradiation when deposited as thin films. Crucially, the ability to adjust the Cu:Ga ratio within the NCs, and its effect on the optical and electronic properties of the NCs was also demonstrated. These results position CuGa$_2$O$_4$ NCs as a novel material for optoelectronic applications, including hole transport and light harvesting.

Semiconducting metal oxides are essential in countless applications, and in recent years oxide nanocrystals (NCs) have emerged as fundamental building blocks for various nanostructures with enhanced properties.[1,2,3,4] Colloidal syntheses for these oxides allow for accurate control of their size, shape, composition, and surface chemistry, enabling their use in applications including photovoltaics, catalysis, plasmonics, electrochromics, sensing, and energy storage.[5,6,7,8,9,10] An extensive library of reactions has been developed for binary metal oxide NCs. However, significantly less research has been conducted on the colloidal synthesis of ternary oxides, due to the increased synthetic challenges of needing to combine multiple precursors with different reactivities. It is worth mentioning that strategies to partially circumvent these challenges have started to appear.[11,12] Ternary oxides (such as perovskites, spinels, delafossites *etc.*) are particularly appealing as the presence of two cation sites allows intrinsic tuning of the materials stoichiometry,[13,14] and additional flexibility when incorporating dopants.[15,16] As such, ternary oxide NCs hold great promise for improving oxide-based devices. For example, ternary oxides have shown enhanced performances in catalysis,[17,18,19,20,21] and optoelectronics,[22,23,24] making their synthesis highly desirable.

Among the various ternary oxides, spinels have demonstrated excellent potential and versatility.[25] Spinel oxides have the general formula AB_2O_4, with the archetypal compound being $MgAl_2O_4$, and in the most common structures A is a divalent cation (e.g. Cu^{2+}, Zn^{2+}, Co^{2+}) and B is a trivalent cation (e.g. Ga^{3+}, Fe^{3+}, Cr^{3+}). Other combinations of cations of different valency are also possible. Many spinel oxides are semiconductors with excellent optoelectronic properties–key compounds include $ZnFe_2O_4$, $CuFe_2O_4$, and $MnCo_2O_4$–and as such they are appealing for the aforementioned applications.[25,26] Spinel oxide NCs with gallium as the trivalent cation, such as $CuGa_2O_4$, $ZnGa_2O_4$ and $FeGa_2O_4$, are largely unexplored, despite their proven use in catalysis, plasmonics and optoelectronics.[13,27,28,29]

Due to the promise of spinel oxides, and the lack of research on Ga-based spinels, here we present the first colloidal synthesis of copper gallate ($CuGa_2O_4$, CGO) NCs. We demonstrate phase-pure $CuGa_2O_4$ NCs with a band gap of ~2.5 eV and strong p-type character. We also show how the stoichiometry can be controlled by adjusting the precursor ratio, allowing us to modulate the optical and electronic properties. Importantly, these NCs can be processed into thin films, which are also photoactive, opening various

possibilities in light harvesting and conversion, photocatalysis, and as hole transport layers for solar cells and LEDs.

CGO NCs were synthesized via a heat-up protocol. Briefly, Cu and Ga acetylacetonates were first dissolved in oleylamine and degassed at 80 °C. Afterwards, the solution was heated to 180 °C under nitrogen and kept at this temperature for 3 hours. The solution was then cooled down to room temperature and the NCs were isolated via conventional precipitation/resuspension protocols. This unusually low nucleation (reaction) temperature for oxide NCs was selected to avoid the reduction of Cu (II) and the formation of Cu (I) oxide or metallic Cu, which were found to form at high reaction temperatures. This is also consistent with existing literature on Cu and Cu_2O NCs.[30,31,32] The presence of additional ligands such as oleic acid, and of alcohols and diols–commonly used in oxide NC syntheses–was also found to trigger the formation of reduced copper impurities.[33,34,35,36] Examples of these reactions are reported in the Supporting Information, Figure S1 and Table S1. As such, a low reaction temperature in neat oleylamine was found to be requisite to the growth of pure $CuGa_2O_4$ NCs.

The x-ray diffraction (XRD) patterns of the NCs show clear peaks ascribed to copper gallate without any visible impurities (Figure 1a). The bulk $CuGa_2O_4$ crystal has a spinel structure (space group *Fd-3m*), wherein oxygens are arranged in a face-centered cubic closed packed lattice, with Ga and Cu occupying octahedral and tetrahedral sites, respectively (Figure 1b). The broad diffraction peaks are indicative of nano-sized crystalline domains. The average crystallite size is 2.5 ± 1.5 nm, which increased to 3.9 ± 1.3 nm after annealing at 500 °C, suggesting good thermal stability of the CGO NCs. This is particularly important when processing the NCs into thin films, which usually require high temperature annealings to decompose the organic ligands. Transmission electron microscopy (TEM) shows that the $CuGa_2O_4$ NCs are spheroidal or slightly elongated, with an average NC size of 3.7 ± 1.1 nm, which is in reasonable agreement with the crystallite size (Figure 1c). High resolution TEM images (Figure 1d, Figure S2) further confirm the size and shape of the NCs, and their crystallinity, with lattice planes clearly visible also in the fast Fourier transform (FFT) images.
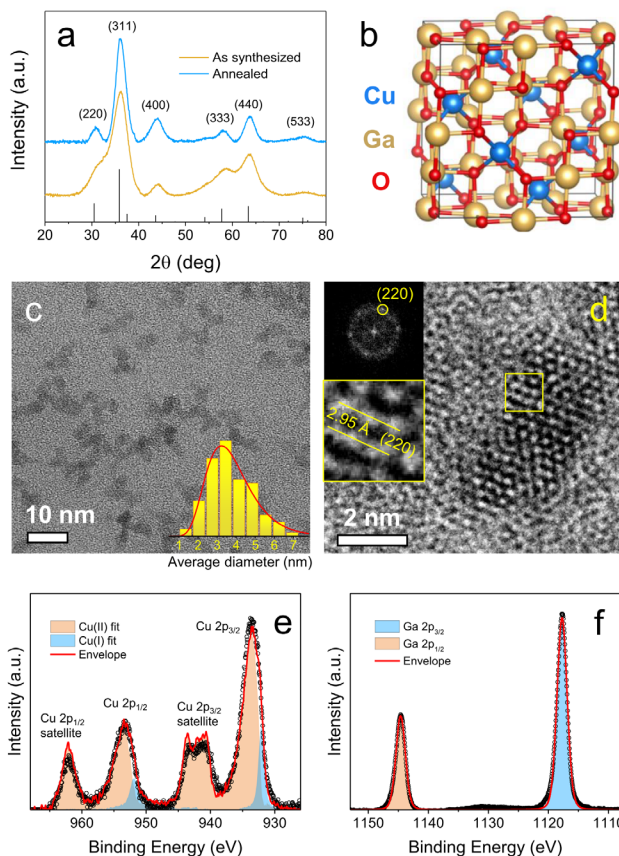
Figure 1. a) XRD pattern of as synthesized and annealed NC powders. The expected peak positions for $CuGa_2O_4$ (ICDD No. 44-0183) are shown. b) Schematic representation of the $CuGa_2O_4$ crystal. c) Low-resolution TEM image (inset: size distribution histogram). d) High-resolution TEM image. e-f) XPS spectra and peak fittings in the Cu 2p (e) and Ga 2p (f) regions.

X-ray photoelectron spectroscopy (XPS) shows clear signatures for Cu, Ga and O (Figure S3). Figure 1e shows the Cu 2p region, which presents distinctive Cu $2p_{1/2}$ and Cu $2p_{3/2}$ peaks at 953.4 eV and 933.7 eV, respectively (spin-orbit splitting of 19.7 eV). Fitting these peaks according to the expected peaks for Cu (I) and Cu (II) oxides shows that copper is mainly present in its 2+ state.[37] Satellite "shake-up" peaks at 942.3 eV and 961.8 eV further confirm the presence of Cu^{2+}, as expected from copper gallate.[38] Figure 2f shows the Ga 2p region demonstrating Ga $2p_{1/2}$ (1144.6 eV) and Ga $2p_{3/2}$ (1117.7 eV) components with a spin-orbit splitting 26.9 eV, indicating the presence of Ga^{3+}.[38, 39] The O 1s region displays a typical asymmetric peak with a main component (530.5 eV) attributed

to oxygen within an oxide lattice. The components at higher binding energies can be ascribed to hydroxides and organic carbonyl/carboxyl species (Figure S3). Compositional analysis via XPS provides a Cu:Ga ratio of 34.4% Cu: 65.6% Ga, which matches well the expected 0.5:1 ratio, and indicates near stoichiometric NCs. Very similar values are obtained with EDX analysis. It is important to highlight that this ratio was obtained starting from a precursor mixture slightly richer in copper (Cu:Ga = 0.6:1) to account for the different reactivity of the precursors (*vide infra*). Collectively, these data suggest that phase pure spinel $CuGa_2O_4$ NCs have been synthesized.

Theoretical models and experiments were combined to assess the optical and electronic properties of the NCs. We first performed density functional theory (DFT) calculations for the bulk, focusing on the ground state electronic structure (Figure 2a). From the band structure and density of states (DOS), we obtained a direct bandgap E_g of ~3 eV for bulk $CuGa_2O_4$ (at the G point), which is just ~55 meV wider than the indirect bandgap. The system also exhibits intrinsic *p*-type behavior with the Fermi level (E_F) being degenerate with the top of the valence band. The electronic states close to the Fermi energy have a majority Cu-O character, while Ga-O states dominate the lowest conduction states. Experimentally, $CuGa_2O_4$ NCs show a sharp absorption onset at ~500 nm, resulting in a bandgap of ~2.5 eV, lower than the predicted theoretical value (Figure 2b). In addition, the presence of an absorption tail extending from the band gap can be seen, possibly related to the presence of in-gap defect states. A picture of the colloidal suspension shows a typical orange-brownish color. The *p*-type nature of the synthesized NCs is confirmed using valence band (VB) XPS (Figure 2c) and Mott-Schottky (M-S, Figure 2d) analyses. The VB edge is detected ~0.6 eV away from the E_F, which together with a band gap of 2.5 eV, suggests a strong *p*-type character. This is corroborated by the negative slope observed in the M-S plot, also distinctive of *p*-type semiconductors.[40]
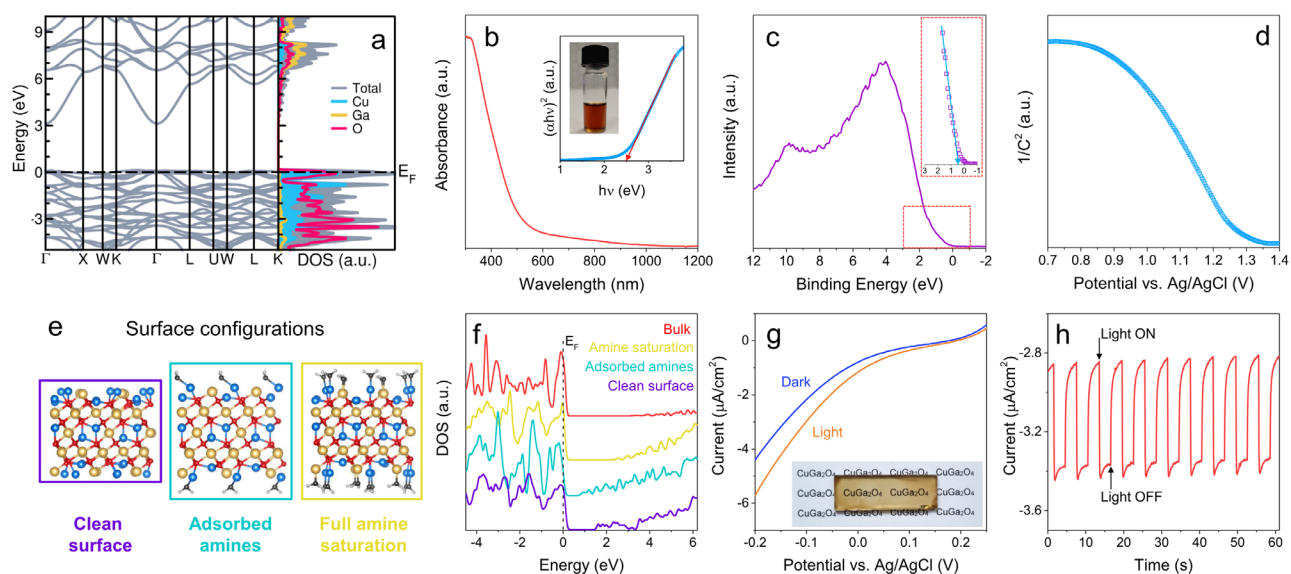
Figure 2. Optical and electronic characterization. a) Calculated band structure and density of states (DOS) for bulk $CuGa_2O_4$. b) Optical absorption spectra of a NC suspension. The inset shows the respective Tauc plot and a photo of the colloidal suspension. c) Valence band XPS spectrum. d) Mott-Schottky plot. e) Computational models of a surface with or without adsorbed amines. f) Calculated DOS for the three models, and comparison with the bulk DOS. g) Linear sweep voltammetry of a $CuGa_2O_4$ NC film in dark and under 455 nm light. The inset shows a photo of the film. h) Photoresponse of the $CuGa_2O_4$ film under pulsed illumination at -0.2 V vs. Ag/AgCl.

To understand the lower band gap of our NCs compared to the expected value for the bulk, we investigated the role of surfaces through the simulation of a 1.1 nm thick slab. The bulk crystal was cleaved along the Cu-terminated (111) surface, as shown schematically in Figure 2e. After full atomic relaxation, the electronic ground state was obtained and summarized in Figure 2f (purple curve). The system maintains a *p*-type character, but the surface termination imparts a different distribution of in-gap states compared to the bulk. Ga-derived empty states appear close to the bottom of the conduction band. Even when adding adsorbed amines (abundant in our reaction, Figure S4) to partially saturate the dangling bonds of the clean surface, Ga defect states are predominant (cyan trace in Figure 2f). Therefore, neither the atomic relaxation nor the

6

amine moieties fully saturate the dangling bond of the outermost Ga atoms. The net effect of these surface contributions is a reduction in the band gap. In an ideal case, where all surface cations are saturated with amines (yellow trace), the band gap is found to be emptied from defect states, although it remains lower than the predicted bulk value (red trace). These simulations highlight the important role of surfaces and related defects, especially in colloidal NCs where the surface/bulk ratio is large, and different facets may be exposed.

The semiconducting nature of the NCs and their band gap in the visible range make them attractive for optoelectronic applications. To demonstrate their photoactivity, we performed photoelectrochemical measurements under blue light illumination on thin film assemblies of the NCs deposited on transparent electrodes from purified NC inks (see Figure S5-S7 for related characterizations). $CuGa_2O_4$ NCs are clearly photoactive, showing distinct photocurrent and reversible signals under chopped illumination (Figure 2g,h and Figure S8). The negative (cathodic) photocurrents observed at negative voltages further confirm the p-type nature of the NCs. These results highlight the promise of these NCs for light-driven applications, such as photocatalysis and optoelectronics.

A key advantage of ternary oxides is the ability to modulate their properties by varying the ratio between the cations.[13,41] We therefore investigated the synthesis of CGO NCs in copper-rich and copper-deficient conditions. Figure 3a shows the XRD patterns of samples prepared with Cu:Ga precursor ratios between 0.33:1 and 1:1. The samples are labeled Cu*X* where *X* is the Cu:Ga nominal ratio. All samples show a diffraction pattern matching copper gallate, however the most copper-rich sample also shows an additional peak at 48.7 ° and shoulders at 38.9 ° and ~66 °, all ascribed to CuO impurities (ICDD: 00-045-0937, marked with stars in Figure 3a). These impurities can be inferred also in the Cu*0.75* sample due to asymmetry in some of the diffraction peaks, and become more distinct in the annealed powders (Figure S9). Importantly, XPS analysis shows additional signatures in the valence band for these two samples at ~12 eV (Figure 3b, star mark), a shifted VB edge almost coinciding with the Fermi energy (Figure S10), and an additional component in the O 1s peak ascribed to Cu-O bonds in CuO (Figure S11).[42,43,44] The experimental Cu:Ga ratios are shown in Figure 3c. All samples have an experimental Cu% lower than the expected value based on precursor loading. Interestingly, the efficiency of Cu

incorporation in relation to precursor amount is very low (~40%) in the Cu*0.33* sample, it increases to ~70% in the Cu*0.5* sample and then it stabilizes to ~90% and above for higher Cu loadings (Table S2). These results suggest that the $CuGa_2O_4$ crystal allows highly copper deficient formulations, however even slightly copper-rich samples result in copper oxide impurities.
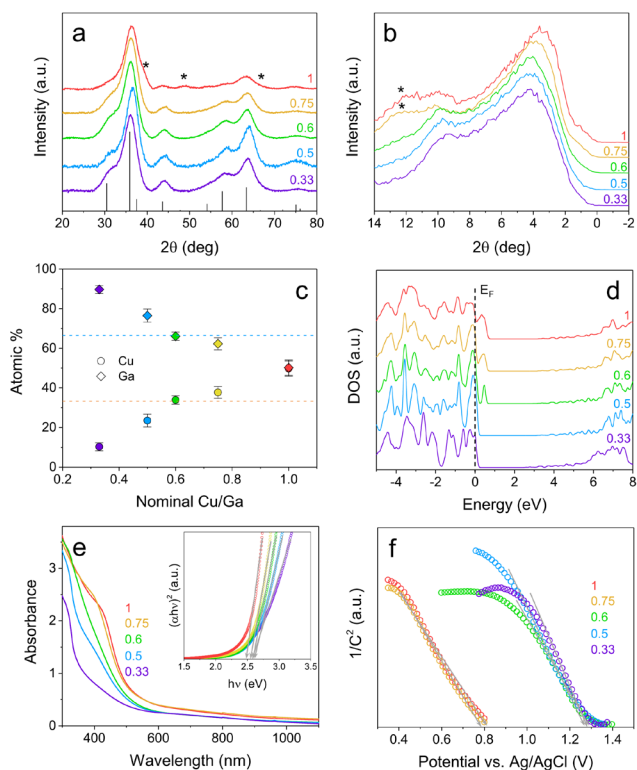

Figure 3. Stoichiometry control. a) XRD patterns. b) Valence band XPS. c) Compositional analysis. Horizontal lines highlight stoichiometric $CuGa_2O_4$ (Cu, orange; Ga, blue). d) Calculated DOS. e) Absorption spectra (Tauc plots as inset). f) Mott-Schottky plots. The legends show the Cu:Ga nominal ratio.

From our computational models, increasingly copper-rich formulations cause an increase in the number of empty acceptor-like states close to the valence band, which narrow the band gap (Figure 3d). Cu acts as an effective *p*-type dopant that shifts the Fermi level deep into the valence band. In copper poor (gallium rich) conditions this scenario is reversed, with less shallow in-gap states and a slightly wider band gap. The optical properties of the synthesized NCs are shown Figure 3e. In agreement with our

simulations, higher copper loadings induce a red-shifted absorption onset and a more pronounced sub-bandgap absorption tail. CuO has a low band gap (~1.4 eV), and therefore CuO impurities in the *Cu1* sample also contribute to this absorption tail. However, the band gap from Tauc analysis does not change significantly, remaining in the 2.5-2.6 eV range. Mott-Schottky analysis showed that all samples retain their *p*-type character regardless of the Cu:Ga ratio. Notably, there is a clear change in the flat band potential (the difference between the material's Fermi energy and the electrochemical potential of the electrolyte).[40] Copper-rich samples show a flat band potential of ~0.8 V vs. Ag/AgCl, while stoichiometric and Ga-rich samples have a flat band potential of ~1.3 V. This ~0.5 V shift is consistent with the shift in the energy difference between the VB edge and the Fermi level, that ranges between ~0.6 eV for stoichiometric and Ga-rich samples, and <0.2 eV for Cu-rich samples (Figure S10). Collectively, these results highlight the strong link between composition and optical properties in copper gallate NCs. As such, accessing specific stoichiometries in this material provides a powerful means to fine tune their properties.

In conclusion, we have presented the synthesis and characterization of small (<5 nm) $CuGa_2O_4$ spinel colloidal NCs. By careful control and optimization of the reaction conditions, we could avoid the formation of reduced copper, obtaining phase pure NCs. Combining spectroscopic and electrochemical characterizations we demonstrated their semiconducting nature, strong p-type character and photoresponse to visible light. DFT calculations were used to assess the electronic structure of this material with specific surface-ligand interactions, which account for the lower-than-expected band gap measured experimentally. We also demonstrated the synthesis of non-stoichiometric compositions which provide an accessible experimental handle on material properties. This, in addition to the ability to process these NCs into thin films, positioning copper gallate as a novel spinel oxide for various optoelectronic applications.

Supporting Information

Experimental methods, and additional XRD, TEM, SEM, UV-Vis, XPS, FTIR and photoelectrochemical characterizations.

Acknowledgements

References

1. Y.-w. Jun, J.-s. Choi and J. Cheon, *Angewandte Chemie International Edition*, 2006, **45**, 3414-3439.
2. M. Cargnello, T. R. Gordon and C. B. Murray, *Chemical Reviews*, 2014, **114**, 9319-9345.
3. L. Qiao and M. T. Swihart, *Advances in Colloid and Interface Science*, 2017, **244**, 199-266.
4. D. Van den Eynden, R. Pokratath and J. De Roo, *Chemical Reviews*, 2022, **122**, 10538-10572.
5. J. Van Embden, S. Gross, K. Kittilstved and E. Della Gaspera, *Chemical Reviews*, 2022, DOI: 10.1021/acs.chemrev.2c00456
6. X. Liang, S. Bai, X. Wang, X. Dai, F. Gao, B. Sun, Z. Ning, Z. Ye and Y. Jin, *Chemical Society Reviews*, 2017, **46**, 1730-1759.
7. A. Agrawal, S. H. Cho, O. Zandi, S. Ghosh, R. W. Johns and D. J. Milliron, *Chemical Reviews*, 2018, **118**, 3121-3207.
8. P. Losch, W. Huang, E. D. Goodman, C. J. Wrasman, A. Holm, A. R. Riscoe, J. A. Schwalbe and M. Cargnello, *Nano Today*, 2019, **24**, 15-47.
9. Y. T. Guntern, V. Okatenko, J. Pankhurst, S. B. Varandili, P. Iyengar, C. Koolen, D. Stoian, J. Vavra and R. Buonsanti, *ACS Catalysis*, 2021, **11**, 1248-1295.
10. M. Ghini, N. Curreli, A. Camellini, M. Wang, A. Asaithambi and I. Kriegel, *Nanoscale*, 2021, **13**, 8773-8783.
11. D. Jung, L. M. A. Saleh, Z. J. Berkson, M. F. El-Kady, J. Y. Hwang, N. Mohamed, A. I. Wixtrom, E. Titarenko, Y. Shao, K. McCarthy, J. Guo, I. B. Martini, S. Kraemer, E. C. Wegener, P. Saint-Cricq, B. Ruehle, R. R. Langeslay, M. Delferro, J. L. Brosmer, C. H. Hendon, M. Gallagher-Jones, J. Rodriguez, K. W. Chapman, J. T. Miller, X. Duan, R. B. Kaner, J. I. Zink, B. F. Chmelka and A. M. Spokoyny, *Nature Materials*, 2018, **17**, 341-348.
12. C. Gadiyar, A. Loiudice, F. D'Ambra, E. Oveisi, D. Stoian, P. Iyengar, L. Castilla-Amorós, V. Mantella and R. Buonsanti, *Journal of the American Chemical Society*, 2020, **142**, 15931-15940.

13. C. Urso, M. Barawi, R. Gaspari, G. Sirigu, I. Kriegel, M. Zavelani-Rossi, F. Scotognella, M. Manca, M. Prato, L. De Trizio and L. Manna, *Journal of the American Chemical Society*, 2017, **139**, 1198-1206.
14. J. Kim, O. Kendall, J. Ren, B. J. Murdoch, C. F. McConville, J. van Embden and E. Della Gaspera, *ACS Applied Materials & Interfaces*, 2022, **14**, 11768-11778.
15. R. Liu, J. Ren, D. Zhao, J. Ning, Z. Zhang, Y. Wang, Y. Zhong, C. Zheng and Y. Hu, *Inorganic Chemistry Frontiers*, 2017, **4**, 2045-2054.
16. W. Shepherd, L. Melendez, O. Kendall, Y. Liu, B. J. Murdoch, J. van Embden, D. E. Gomez and E. Della Gaspera, *Materials Today Chemistry*, 2022, **26**, 101208.
17. J. Hwang, R. R. Rao, L. Giordano, Y. Katayama, Y. Yu and Y. Shao-Horn, *Science*, 2017, **358**, 751-756.
18. Y. J. Jang, Y. B. Park, H. E. Kim, Y. H. Choi, S. H. Choi and J. S. Lee, *Chemistry of Materials*, 2016, **28**, 6054-6061.
19. D. K. Lee, D. Lee, M. A. Lumley and K.-S. Choi, *Chemical Society Reviews*, 2019, **48**, 2126-2157.
20. S. P. Ratnayake, J. Ren, J. van Embden, C. F. McConville and E. Della Gaspera, *Journal of Materials Chemistry A*, 2021, **9**, 25641-25650.
21. X. Yang, E. A. Fugate, Y. Mueanngern and L. R. Baker, *ACS Catalysis*, 2017, **7**, 177-180.
22. W. Ji, K. Yao and Y. C. Liang, *Advanced Materials*, 2010, **22**, 1763-1766.
23. H. Zhang, H. Wang, W. Chen and A. K. Y. Jen, *Advanced Materials*, 2017, **29**, 1604984.
24. S. S. Shin, E. J. Yeom, W. S. Yang, S. Hur, M. G. Kim, J. Im, J. Seo, J. H. Noh and S. I. Seok, *Science*, 2017, **356**, 167-171.
25. Q. Zhao, Z. Yan, C. Chen and J. Chen, *Chemical Reviews*, 2017, **117**, 10121-10211.
26. Y. Shi, P. F. Ndione, L. Y. Lim, D. Sokaras, T.-C. Weng, A. R. Nagaraja, A. G. Karydas, J. D. Perkins, T. O. Mason, D. S. Ginley, A. Zunger and M. F. Toney, *Chemistry of Materials*, 2014, **26**, 1867-1873.
27. K. Gurunathan, J.-O. Baeg, S. M. Lee, E. Subramanian, S.-J. Moon and K.-j. Kong, *International Journal of Hydrogen Energy*, 2008, **33**, 2646-2652.
28. S. C. Yan, S. X. Ouyang, J. Gao, M. Yang, J. Y. Feng, X. X. Fan, L. J. Wan, Z. S. Li, J. H. Ye, Y. Zhou and Z. G. Zou, *Angewandte Chemie International Edition*, 2010, **49**, 6400-6404.
29. X. Hou, T. Xuan, H. Sun, X. Chen, H. Li and L. Pan, *Solar Energy Materials and Solar Cells*, 2016, **149**, 121-127.
30. M. Yin, C.-K. Wu, Y. Lou, C. Burda, J. T. Koberstein, Y. Zhu and S. O'Brien, *Journal of the American Chemical Society*, 2005, **127**, 9506-9511.
31. H. Guo, Y. Chen, M. B. Cortie, X. Liu, Q. Xie, X. Wang and D.-L. Peng, *The Journal of Physical Chemistry C*, 2014, **118**, 9801-9808.
32. A. Loiudice, P. Lobaccaro, E. A. Kamali, T. Thao, B. H. Huang, J. W. Ager and R. Buonsanti, *Angewandte Chemie International Edition*, 2016, **55**, 5789-5792.
33. E. Della Gaspera, A. S. R. Chesman, J. van Embden and J. J. Jasieniak, *ACS Nano*, 2014, **8**, 9154-9163.
34. D. Ito, S. Yokoyama, T. Zaikova, K. Masuko and J. E. Hutchison, *ACS Nano*, 2014, **8**, 64-75.
35. A. W. Jansons, L. K. Plummer and J. E. Hutchison, *Chemistry of Materials*, 2017, **29**, 5415-5425.
36. P. Wainer, O. Kendall, A. Lamb, S. J. Barrow, A. Tricoli, D. E. Gómez, J. van Embden and E. Della Gaspera, *Chemistry of Materials*, 2019, **31**, 9604-9613.
37. NIST X-ray Photoelectron Spectroscopy Database (https://srdata.nist.gov/xps/Default.aspx)).
38. R. Pilliadugula, C. Nithya and N. Gopala Krishnan, *Nanoscale Advances*, 2020, **2**, 1269-1281.

39. D. A. Zatsepin, D. W. Boukhvalov, A. F. Zatsepin, Y. A. Kuznetsova, D. Gogova, V. Y. Shur and A. A. Esin, *Superlattices and Microstructures*, 2018, **120**, 90-100.
40. A. Hankin, F. E. Bedoya-Lora, J. C. Alexander, A. Regoutz and G. H. Kelsall, *Journal of Materials Chemistry A*, 2019, **7**, 26162-26176.
41. W. Shepherd, M. Wilms, J. van Embden and E. Della Gaspera, *Chemical Communications*, 2019, **55**, 11880-11883.
42. D. Barreca, A. Gasparotto and E. Tondello, *Surface Science Spectra*, 2007, **14**, 41-51.
43. V. Fernandez, D. Kiani, N. Fairley, F.-X. Felpin and J. Baltrusaitis, *Applied Surface Science*, 2020, **505**, 143841.
44. K. Roy and C. S. Gopinath, *Analytical Chemistry*, 2014, **86**, 3683-3687.